Available online at www.sciencedirect.com

ScienceDirect

International Journal of Heat and Mass Transfer 51 (2008) 1979–1995

International Journal of HEAT and MASS TRANSFER

www.elsevier.com/locate/ijhmt

A finite difference method for studying thermal deformation in a 3D thin film exposed to ultrashort pulsed lasers

Suyang Zhang [a], Weizhong Dai [a,*], Haojie Wang [a], Roderick V.N. Melnik [b]

[a] Mathematics and Statistics, College of Engineering and Science, Louisiana Tech University, Ruston, LA 71272, USA
[b] Mathematical Modelling and Computational Sciences, Wilfrid Laurier University, Waterloo, ON, Canada N2L 3C5

Received 5 April 2007; received in revised form 7 June 2007
Available online 14 September 2007

Abstract

Ultrashort pulsed lasers have been attracting worldwide interest in science and engineering communities. Studying the thermal deformation induced by ultrashort pulsed lasers is important for preventing thermal damage. This article presents a new numerical method for studying thermal deformation in a 3D thin film exposed to ultrashort pulsed lasers. The method is obtained based on the parabolic two-step model and implicit finite difference schemes on a staggered mesh. It accounts for the coupling effect between lattice temperature and strain rate, as well as for the hot electron-blast effect in momentum transfer. In particular, a fourth-order compact scheme is developed for evaluating those stress derivatives in the dynamic equations of motion. The method allows us to avoid non-physical oscillations in the solution. Its performance is demonstrated by a numerical example.

1. Introduction

Ultrafast lasers with pulse durations of the order of sub-picoseconds to femtoseconds possess exclusive capabilities in limiting the undesirable spread of the thermal process zone in the heated sample [1]. The application of ultra-short-pulsed lasers includes structural monitoring of thin metal films [2,3], laser micromachining and patterning [4], structural tailoring of microfilms [5], and laser synthesis and processing in thin-film deposition [6]. Recent applications of ultrashort-pulsed lasers have been in different disciplines such as physics, chemistry, biology, medicine, and optical technology [7–10]. The non-contact nature of femtosecond lasers has made them an ideal candidate for precise thermal processing of functional nanophase materials [1].

Success of high-energy ultrashort-pulsed lasers in real applications relies on three factors [1]: (1) well characterized pulse width, intensity and experimental techniques; (2) reliable microscale heat transfer models; and (3) prevention of thermal damage. Up to date, a number of models that focus on heat transfer in the context of ultrashort-pulsed lasers have been developed [11–23]. However, only a few mathematical models for studying thermal deformation induced by ultrashort pulsed lasers have been developed [1,24–26]. Tzou and his colleagues [1] presented a one-dimensional model in a double-layered thin film. The model was solved using a differential-difference approach. Chen and his colleagues [24] considered a two-dimensional axisymmetric cylindrical thin film and proposed an explicit finite difference method by adding an artificial viscosity term to eliminate numerical oscillations. Recently, we have developed a new method for studying thermal deformation in 2D thin films exposed to ultrashort pulsed lasers [27–29]. The method is obtained based on the parabolic two-step heat transport equations and implicit finite difference schemes on a staggered mesh. It accounts for the coupling effect between lattice temperature and strain rate, as well as for the hot electron-blast effect in momentum transfer. Numerical results show that there are no numerical oscillations in the solution. Unfortunately, when applied to a 3D thin film case, the non-physical oscillations in the stress (σ_z) appear in the solution. This is probably

* Corresponding author. Tel.: +1 318 257 3301; fax: +1 318 257 2562.
E-mail address: dai@coes.latech.edu (W. Dai).

0017-9310/$ - see front matter
doi:10.1016/j.ijheatmasstransfer.2007.06.040

Nomenclature

C_{e0}	electron heat capacity
C_l	lattice heat capacity
G	electron–lattice coupling factor
J	laser fluence
K	bulk modulus
K_e	thermal conductivity
R	surface reflectivity
T_e	electron temperature
T_l	lattice temperature
t, t_n	time
t_p	laser pulse duration
u, v, w	displacements in the x, y and z directions, respectively
$u^n(i,j,k)$	numerical solution of $u(x_i, y_j, z_k, t_n)$
v_1, v_2, v_3	velocity components in the x, y and z directions, respectively
x, y, z	Cartesian coordinates
z_s	optical penetration depth
r_s	spatial profile parameter of laser
α_T	thermal expansion coefficient
$\Delta t, \Delta x, \Delta y, \Delta z$	time increment and spatial step sizes, respectively
Δ_{-t}, δ_x	finite difference operators
$\varepsilon_x, \varepsilon_y, \varepsilon_z$	normal strains in the x, y and z directions, respectively
Λ	electron-blast coefficient
$\gamma_{xy}, \gamma_{xz}, \gamma_{yz}$	shear strain
λ	Lame's coefficient
μ	Lame's coefficient
ρ	density
$\sigma_x, \sigma_y, \sigma_z$	normal stresses in the x, y and z directions, respectively
$\sigma_{xy}, \sigma_{xz}, \sigma_{yz}$	shear stresses in the x, y and z directions, respectively

because we used a relatively coarse grid in the computation. However, a finer mesh increased dramatically the computation cost. In this article, we extend our research to a 3D thin film case by developing a fourth-order compact finite difference scheme for solving the dynamic equations of motion. Result shows that the non-physical oscillations disappear.

2. Mathematical model

Consider a three-dimensional thin film in Cartesian coordinates, which is exposed to ultrashort pulsed lasers, as shown in Fig. 1. The governing equations for studying thermal deformation in the thin film can be expressed as follows:

(1) *Dynamic equations of motion* [1,24,27,30].

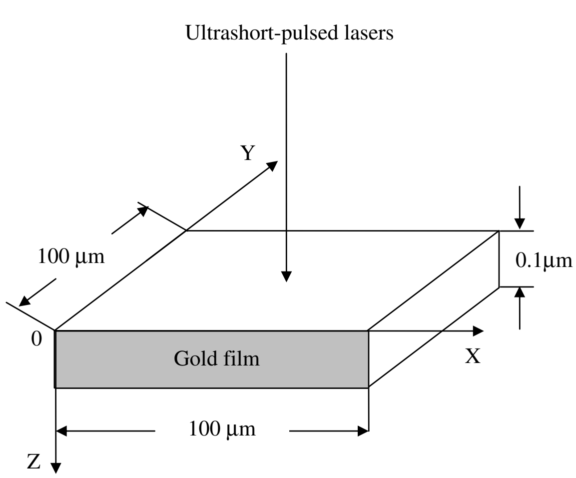

Fig. 1. A 3D thin film with the dimension of 100 µm × 100 µm × 0.1µm, irradiated by ultrashort-pulsed lasers.

$$\rho\frac{\partial^2 u}{\partial t^2} = \frac{\partial \sigma_x}{\partial x} + \frac{\partial \sigma_{xy}}{\partial y} + \frac{\partial \sigma_{xz}}{\partial z} + 2\Lambda T_e \frac{\partial T_e}{\partial x}, \quad (1)$$

$$\rho\frac{\partial^2 v}{\partial t^2} = \frac{\partial \sigma_{xy}}{\partial x} + \frac{\partial \sigma_y}{\partial y} + \frac{\partial \sigma_{yz}}{\partial z} + 2\Lambda T_e \frac{\partial T_e}{\partial y}, \quad (2)$$

$$\rho\frac{\partial^2 w}{\partial t^2} = \frac{\partial \sigma_{xz}}{\partial x} + \frac{\partial \sigma_{yz}}{\partial y} + \frac{\partial \sigma_z}{\partial z} + 2\Lambda T_e \frac{\partial T_e}{\partial z}, \quad (3)$$

$$\sigma_x = \lambda(\varepsilon_x + \varepsilon_y + \varepsilon_z) + 2\mu\varepsilon_x - (3\lambda + 2\mu)\alpha_T(T_l - T_0), \quad (4a)$$

$$\sigma_y = \lambda(\varepsilon_x + \varepsilon_y + \varepsilon_z) + 2\mu\varepsilon_y - (3\lambda + 2\mu)\alpha_T(T_l - T_0), \quad (4b)$$

$$\sigma_z = \lambda(\varepsilon_x + \varepsilon_y + \varepsilon_z) + 2\mu\varepsilon_z - (3\lambda + 2\mu)\alpha_T(T_l - T_0), \quad (4c)$$

$$\sigma_{xy} = \mu\gamma_{xy}, \quad \sigma_{xz} = \mu\gamma_{xz}, \quad \sigma_{yz} = \mu\gamma_{yz}, \quad (4d)$$

$$\varepsilon_x = \frac{\partial u}{\partial x}, \quad \varepsilon_y = \frac{\partial v}{\partial y}, \quad \varepsilon_z = \frac{\partial w}{\partial z}, \quad (4e)$$

$$\gamma_{xy} = \frac{\partial u}{\partial y} + \frac{\partial v}{\partial x}, \quad \gamma_{xz} = \frac{\partial u}{\partial z} + \frac{\partial w}{\partial x}, \quad \gamma_{yz} = \frac{\partial v}{\partial z} + \frac{\partial w}{\partial y}. \quad (4f)$$

Here, u, v, w are the displacements in the x, y, z directions, respectively; ε_x, ε_y and ε_z are the normal strains in the x, y and z directions, respectively; γ_{xy} is the shear strain in the xy direction, γ_{xz} is the shear strain in the xz direction, γ_{yz} is the shear strain in the yz direction; σ_x, σ_y and σ_z are the normal stresses in the x, y and z directions, respectively; σ_{xy} is the shear stress in the xy direction, σ_{xz} is the shear stress in the xz direction, σ_{yz} is the shear stress in the yz direction; T_e and T_l are electron and lattice temperatures, respectively; T_0 is the initial temperature; ρ is density; Λ is electron-blast coefficient; $\lambda = K - \frac{2}{3}\mu$ [31] and μ are Lame's coefficients; and α_T is the thermal expansion coefficient.

(2) *Energy equations* [1,24,27,32].

$$C_e(T_e)\frac{\partial T_e}{\partial t} = \frac{\partial}{\partial x}\left(k_e(T_e,T_l)\frac{\partial T_e}{\partial x}\right) + \frac{\partial}{\partial y}\left(k_e(T_e,T_l)\frac{\partial T_e}{\partial y}\right) + \frac{\partial}{\partial z}\left(k_e(T_e,T_l)\frac{\partial T_e}{\partial z}\right) - G(T_e - T_l) + Q, \quad (5)$$

$$C_l\frac{\partial T_l}{\partial t} = G(T_e - T_l) - (3\lambda + 2\mu)\alpha_T T_0 \frac{\partial}{\partial t}(\varepsilon_x + \varepsilon_y + \varepsilon_z), \quad (6)$$

where the heat source is given by

$$Q(x,y,z,t) = 0.94J\frac{1-R}{t_p z_s}\exp\left[-\frac{z}{z_s} - \frac{(x-x_0)^2 + (y-y_0)^2}{r_s^2} - 2.77\left(\frac{t-2t_p}{t_p}\right)^2\right]. \quad (7)$$

Here, $C_e(T_e) = C_{e0}(\frac{T_e}{T_0})$ is the electron heat capacity, $k_e(T_e,T_l) = k_0(\frac{T_e}{T_l})$ is the thermal conductivity, G is the electron-lattice coupling factor, C_l is the lattice heat capacities, respectively; Q is energy absorption rate; J is laser fluence; R is surface reflectivity; $t_p$is laser pulse duration; z_s is optical penetration depth; r_s is spatial profile parameter. Eqs. (5) and (6) are often referred to as parabolic two-step heat transport equations.

The boundary conditions are assumed to be stress free and thermally insulated:

$$\sigma_x = 0, \quad \sigma_{xy} = 0, \quad \sigma_{xz} = 0, \quad \text{at } x = 0,\ L_x, \quad (8a)$$

$$\sigma_y = 0, \quad \sigma_{xy} = 0, \quad \sigma_{yz} = 0, \quad \text{at } y = 0,\ L_y, \quad (8b)$$

$$\sigma_z = 0, \quad \sigma_{xz} = 0, \quad \sigma_{yz} = 0, \quad \text{at } z = 0,\ L_z, \quad (8c)$$

$$\frac{\partial T_e}{\partial \vec{n}} = 0, \quad \frac{\partial T_l}{\partial \vec{n}} = 0, \quad (9)$$

where $\vec{n}$ is the unit outward normal vector on the boundary. It should be pointed out that insulated boundaries are imposed due to the assumption that there are no heat losses from the film surfaces in the short time response.

The initial conditions are assumed to be

$$T_e = T_l = T_0, \quad u = v = w = 0,$$
$$u_t = v_t = w_t = 0, \quad \text{at } t = 0. \quad (10)$$

3. Finite difference method

Using a similar argument as that in [27–29], we introduce three velocity components v_1, v_2 and v_3 into the model and re-write the dynamic equations of motion, Eqs. (1)–(4), as follows:

$$v_1 = \frac{\partial u}{\partial t}, \quad v_2 = \frac{\partial v}{\partial t}, \quad v_3 = \frac{\partial w}{\partial t}, \quad (11)$$

$$\rho\frac{\partial v_1}{\partial t} = \frac{\partial \sigma_x}{\partial x} + \frac{\partial \sigma_{xy}}{\partial y} + \frac{\partial \sigma_{xz}}{\partial z} + 2\Lambda T_e\frac{\partial T_e}{\partial x}, \quad (12)$$

$$\rho\frac{\partial v_2}{\partial t} = \frac{\partial \sigma_{xy}}{\partial x} + \frac{\partial \sigma_y}{\partial y} + \frac{\partial \sigma_{yz}}{\partial z} + 2\Lambda T_e\frac{\partial T_e}{\partial y}, \quad (13)$$

$$\rho\frac{\partial v_3}{\partial t} = \frac{\partial \sigma_{xz}}{\partial x} + \frac{\partial \sigma_{yz}}{\partial y} + \frac{\partial \sigma_z}{\partial z} + 2\Lambda T_e\frac{\partial T_e}{\partial z}, \quad (14)$$

$$\frac{\partial \varepsilon_x}{\partial t} = \frac{\partial v_1}{\partial x}, \quad \frac{\partial \varepsilon_y}{\partial t} = \frac{\partial v_2}{\partial y}, \quad \frac{\partial \varepsilon_z}{\partial t} = \frac{\partial v_3}{\partial z}, \quad (15a)$$

$$\frac{\partial \gamma_{xy}}{\partial t} = \frac{\partial v_1}{\partial y} + \frac{\partial v_2}{\partial x}, \quad \frac{\partial \gamma_{xz}}{\partial t} = \frac{\partial v_1}{\partial z} + \frac{\partial v_3}{\partial x}, \quad \frac{\partial \gamma_{yz}}{\partial t} = \frac{\partial v_2}{\partial z} + \frac{\partial v_3}{\partial y}. \quad (15b)$$

To develop a finite difference scheme, we first construct a staggered grid as shown in Fig. 2, where v_1 is placed at $(x_{i+\frac{1}{2}}, y_j, z_k)$, v_2 is placed at $(x_i, y_{j+\frac{1}{2}}, z_k)$, v_3 is placed at $(x_i, y_j, z_{k+\frac{1}{2}})$, γ_{xy} and σ_{xy} are placed at $(x_{i+\frac{1}{2}}, y_{j+\frac{1}{2}}, z_k)$, γ_{xz} and σ_{xz} are placed at $(x_{i+\frac{1}{2}}, y_j, z_{k+\frac{1}{2}})$, γ_{yz} and σ_{yz} are placed at $(x_i, y_{j+\frac{1}{2}}, z_{k+\frac{1}{2}})$, while ε_x, ε_y, ε_z, σ_x, σ_y, σ_z, T_e and T_l are at (x_i, y_j, z_k). Here, i, j and k are indices with $1 \leqslant i \leqslant N_x + 1$, $1 \leqslant j \leqslant N_y + 1$ and $1 \leqslant k \leqslant N_z + 1$. We denote $v_1^n(i+\frac{1}{2}, j, k)$,$v_2^n(i, j+\frac{1}{2}, k)$ and $v_3^n(i, j, k+\frac{1}{2})$ as numerical approximations of $v_1((i+\frac{1}{2})\Delta x, j\Delta y, k\Delta z, n\Delta t)$, $v_2(i\Delta x, (j+\frac{1}{2})\Delta y, k\Delta z, n\Delta t)$ and $v_3(i\Delta x, j\Delta y, (k+\frac{1}{2})\Delta z, n\Delta t)$, respectively, where $\Delta t, \Delta x$, Δy and Δz are time increment and spatial step sizes, respectively. Similar notations are used for other variables. Furthermore, we introduce the finite difference operators, Δ_{-t} and δ_x, as follows:

$$\Delta_{-t}u_i^n = u_i^n - u_i^{n-1}, \quad \delta_x u_i^n = u^n_{i+\frac{1}{2}} - u^n_{i-\frac{1}{2}}.$$

It should be pointed out that the staggered-grid method is often employed in computational fluid dynamics to prevent the solution from oscillations [33]. For example, if v_1 and ε_x in Eq. (15a) are placed at a same location, employing a central finite difference scheme may produce a velocity component v_1, a wave solution, implying oscillation.

To avoid non-physical oscillations in the solution, we develop a fourth-order compact finite difference scheme for stress derivatives $\frac{\partial \sigma_x}{\partial x}$, $\frac{\partial \sigma_{xy}}{\partial y}$, $\frac{\partial \sigma_{xz}}{\partial z}$, etc. in Eqs. (12)–(15). To this end, we let

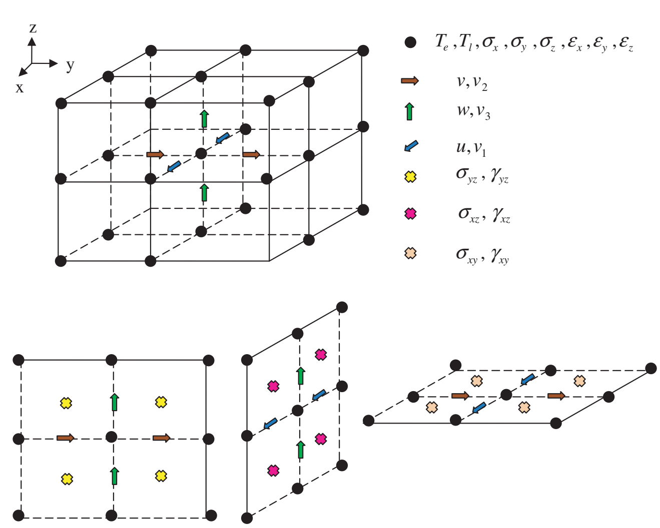

Fig. 2. A 3D staggered mesh and locations of variables.

$$a\frac{\partial\sigma_x(i-1)}{\partial x}+b\frac{\partial\sigma_x(i)}{\partial x}+a\frac{\partial\sigma_x(i+1)}{\partial x}=\frac{\sigma_x\left(i+\frac{1}{2}\right)-\sigma_x\left(i-\frac{1}{2}\right)}{\Delta x},\quad 2+\tfrac{1}{2}\leqslant i\leqslant N_x-\tfrac{1}{2},\tag{16}$$

where a and b are unknown constants. Here, we omit indices j,k, and n for simplicity. Using the Taylor series expansion, we obtain

$$\sigma_x\left(i+\tfrac{1}{2}\right)=\sigma_x(i)+\frac{\Delta x}{2}\frac{\partial\sigma_x(i)}{\partial x}+\frac{\Delta x^2}{2!2^2}\frac{\partial^2\sigma_x(i)}{\partial x^2}+\frac{\Delta x^3}{3!2^3}\frac{\partial^3\sigma_x(i)}{\partial x^3}+\frac{\Delta x^4}{4!2^4}\frac{\partial^4\sigma_x(i)}{\partial x^4}+\mathrm{O}(\Delta x^5),\tag{17a}$$

$$\sigma_x\left(i-\tfrac{1}{2}\right)=\sigma_x(i)-\frac{\Delta x}{2}\frac{\partial\sigma_x(i)}{\partial x}+\frac{\Delta x^2}{2!2^2}\frac{\partial^2\sigma_x(i)}{\partial x^2}-\frac{\Delta x^3}{3!2^3}\frac{\partial^3\sigma_x(i)}{\partial x^3}+\frac{\Delta x^4}{4!2^4}\frac{\partial^4\sigma_x(i)}{\partial x^4}+\mathrm{O}(\Delta x^5),\tag{17b}$$

$$\frac{\partial\sigma_x(i+1)}{\partial x}=\frac{\partial\sigma_x(i)}{\partial x}+\Delta x\frac{\partial^2\sigma_x(i)}{\partial x^2}+\frac{\Delta x^2}{2}\frac{\partial^3\sigma_x(i)}{\partial x^3}+\frac{\Delta x^3}{3!}\frac{\partial^4\sigma_x(i)}{\partial x^4}+\mathrm{O}(\Delta x^4),\tag{17c}$$

$$\frac{\partial\sigma_x(i-1)}{\partial x}=\frac{\partial\sigma_x(i)}{\partial x}-\Delta x\frac{\partial^2\sigma_x(i)}{\partial x^2}+\frac{\Delta x^2}{2}\frac{\partial^3\sigma_x(i)}{\partial x^3}-\frac{\Delta x^3}{3!}\frac{\partial^4\sigma_x(i)}{\partial x^4}+\mathrm{O}(\Delta x^4).\tag{17d}$$

Substituting the above equations into Eq. (16) and comparing the corresponding terms, we obtain

$$2a+b=1,\quad a=\frac{1}{24},\quad b=\frac{11}{12},\tag{18}$$

with truncation error of $\mathrm{O}(\Delta x^4)$. It should be pointed out that the dissipative term $\frac{\partial^3\sigma_x(i)}{\partial x^3}$ has been eliminated from the truncation error. Hence, $\frac{\partial\sigma_x}{\partial x}$ can be obtained by solving the following tridiagonal system

$$\frac{1}{24}\frac{\partial\sigma_x(i-1)}{\partial x}+\frac{11}{12}\frac{\partial\sigma_x(i)}{\partial x}+\frac{1}{24}\frac{\partial\sigma_x(i+1)}{\partial x}=\frac{\sigma_x(i+\frac{1}{2})-\sigma_x(i-\frac{1}{2})}{\Delta x},\quad 2+\tfrac{1}{2}\leqslant i\leqslant N_x-\tfrac{1}{2},\tag{19}$$

where

$$\frac{\partial\sigma_x(\frac{3}{2})}{\partial x}=\frac{\sigma_x(2)-\sigma_x(1)}{\Delta x},\quad \frac{\partial\sigma_x(N_x+\frac{1}{2})}{\partial x}=\frac{\sigma_x(N_x+1)-\sigma_x(N_x)}{\Delta x}.\tag{20}$$

Using a similar argument, we can evaluate other stress derivatives in Eqs. (12)–(14). Hence, the implicit finite difference schemes for solving Eqs. (12)–(14) can be written as follows:

$$\rho\frac{1}{\Delta t}\Delta_{-t}v_1^{n+1}(i+\tfrac{1}{2},j,k)=\frac{\partial\sigma_x^{n+1}(i+\frac{1}{2},j,k)}{\partial x}+\frac{\partial\sigma_{xy}^{n+1}(i+\frac{1}{2},j,k)}{\partial y}+\frac{\partial\sigma_{xz}^{n+1}(i+\frac{1}{2},j,k)}{\partial z}+\Lambda\frac{1}{\Delta x}\delta_x(T_e^2)^{n+1}(i+\tfrac{1}{2},j,k),\tag{21}$$

$$\rho\frac{1}{\Delta t}\Delta_{-t}v_2^{n+1}(i,j+\tfrac{1}{2},k)=\frac{\partial\sigma_y^{n+1}(i,j+\frac{1}{2},k)}{\partial y}+\frac{\partial\sigma_{xy}^{n+1}(i,j+\frac{1}{2},k)}{\partial x}+\frac{\partial\sigma_{yz}^{n+1}(i,j+\frac{1}{2},k)}{\partial z}+\Lambda\frac{1}{\Delta y}\delta_y(T_e^2)^{n+1}(i,j+\tfrac{1}{2},k),\tag{22}$$

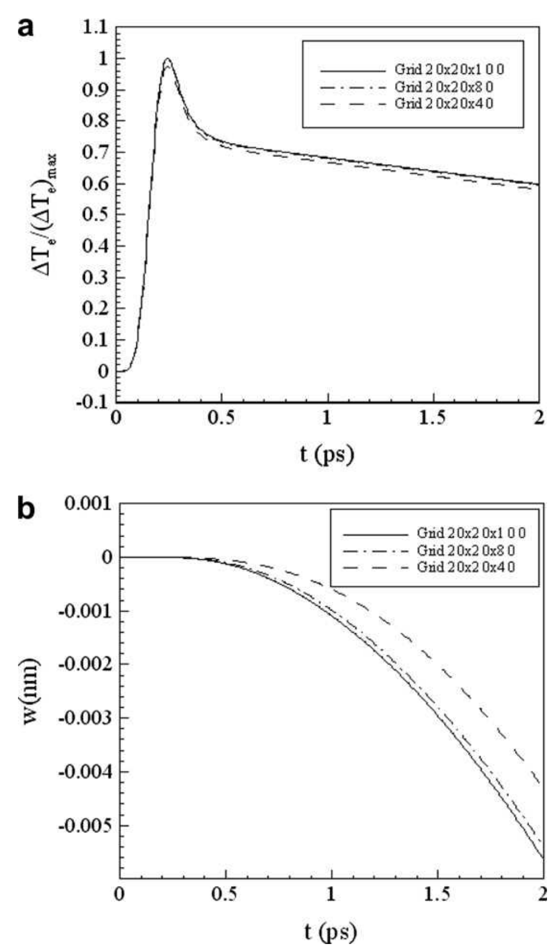

Fig. 3. Change in electron temperature and displacement (w) at the center of top surface versus time for various grids ($20\times20\times40$, $20\times20\times80$, $20\times20\times100$) and laser fluence J of 500 J/m^2.

Table 1
Thermophysical properties

Properties	Unit	Value
ρ	kg/m^3	19,300
Λ	J m^{-3} K^{-2}	70
K	Pa	217×10^9
μ	Pa	27×10^9
α_T	K^{-1}	14.2×10^{-6}
C_{e0}	J/(m^3 K)	2.1×10^4
C_l	J/(m^3 K)	2.5×10^6
G	W/(m^3 K)	2.6×10^{16}
K_e	W/(m K)	315
R		0.93
t_p	s	0.1×10^{-12}
z_s	m	15.3×10^{-9}
r_s	m	1.0×10^{-6}
J	J/m^2	500, 2000

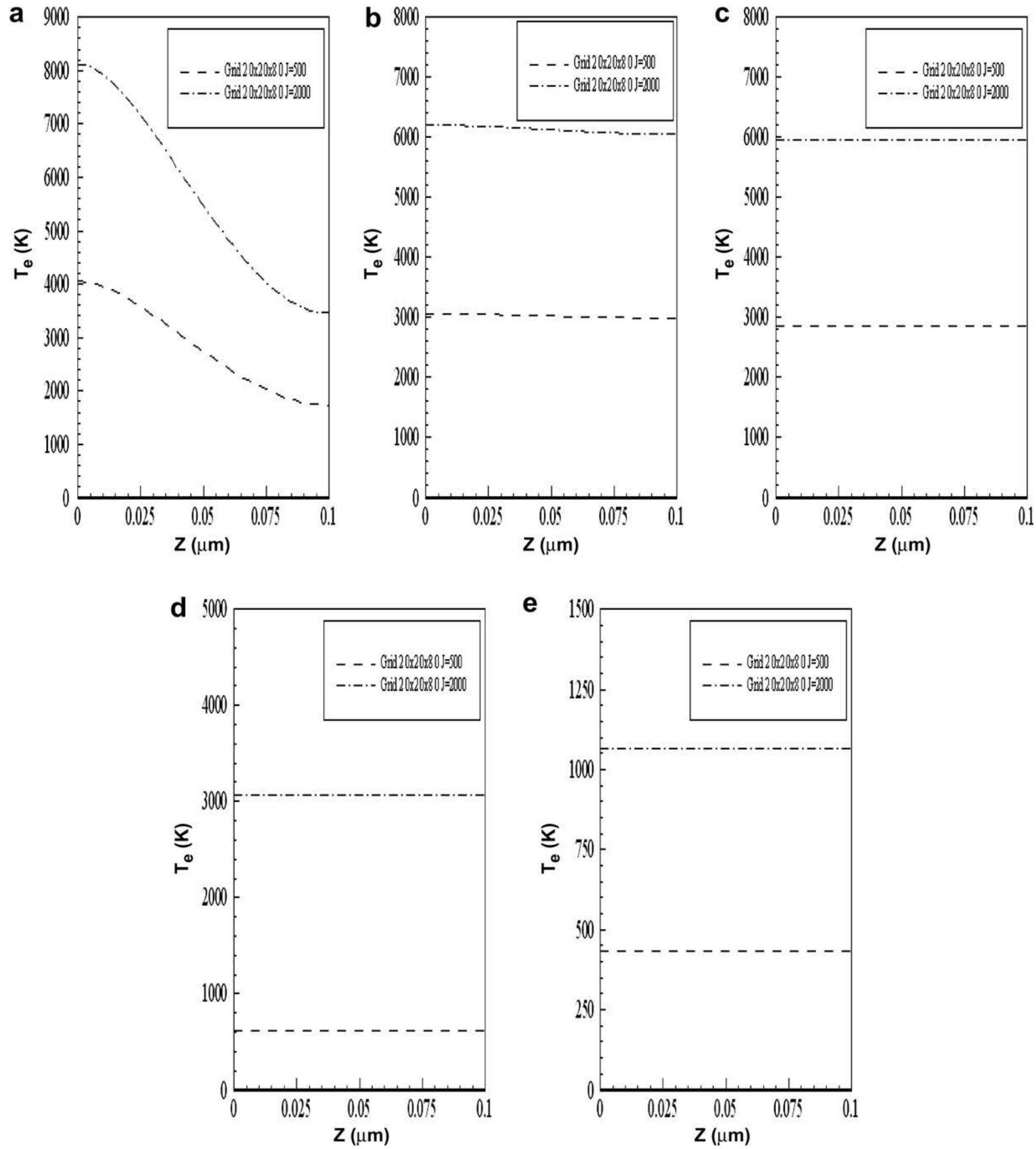

Fig. 4. Electron temperature profiles along z at (x_{center}, y_{center}) at different times: (a) $t = 0.25$ ps, (b) $t = 0.5$ ps, (c) $t = 1$ ps, (d) $t = 10$ ps and (e) $t = 20$ ps with a mesh of $20 \times 20 \times 80$ and two different laser fluences J of 500 J/m^2 and J of 2000 J/m^2.

$$\rho \frac{1}{\Delta t}\Delta_{-t} v_3^{n+1}(i,j,k+\tfrac{1}{2}) = \frac{\partial \sigma_z^{n+1}(i,j,k+\frac{1}{2})}{\partial z} + \frac{\partial \sigma_{xz}^{n+1}(i,j,k+\frac{1}{2})}{\partial x} + \frac{\partial \sigma_{yz}^{n+1}(i,j,k+\frac{1}{2})}{\partial y} + \Lambda \frac{1}{\Delta z}\delta_z (T_e^2)^{n+1}(i,j,k+\tfrac{1}{2}). \quad (23)$$

On the other hand, the finite difference schemes for rest of the governing equations can be seen as generalizations of the schemes described in [27] to the 3D case. We summarize these generalizations below:

$$\frac{1}{\Delta t}\Delta_{-t}\varepsilon_x^{n+1}(i,j,k) = \frac{1}{\Delta x}\delta_x v_1^{n+1}(i,j,k), \quad (24a)$$

$$\frac{1}{\Delta t}\Delta_{-t}\varepsilon_y^{n+1}(i,j,k) = \frac{1}{\Delta y}\delta_y v_2^{n+1}(i,j,k), \quad (24b)$$

$$\frac{1}{\Delta t}\Delta_{-t}\varepsilon_z^{n+1}(i,j,k) = \frac{1}{\Delta z}\delta_z v_3^{n+1}(i,j,k), \quad (24c)$$

$$\frac{1}{\Delta t}\Delta_{-t}\gamma_{xy}^{n+1}(i+\tfrac{1}{2},j+\tfrac{1}{2},k) = \frac{1}{\Delta y}\delta_y v_1^{n+1}(i+\tfrac{1}{2},j+\tfrac{1}{2},k) + \frac{1}{\Delta x}\delta_x v_2^{n+1}(i+\tfrac{1}{2},j+\tfrac{1}{2},k), \quad (25a)$$

$$\frac{1}{\Delta t}\Delta_{-t}\gamma_{xz}^{n+1}(i+\tfrac{1}{2},j,k+\tfrac{1}{2}) = \frac{1}{\Delta z}\delta_z v_1^{n+1}(i+\tfrac{1}{2},j,k+\tfrac{1}{2}) + \frac{1}{\Delta x}\delta_x v_3^{n+1}(i+\tfrac{1}{2},j,k+\tfrac{1}{2}), \tag{25b}$$

$$\frac{1}{\Delta t}\Delta_{-t}\gamma_{yz}^{n+1}(i,j+\tfrac{1}{2},k+\tfrac{1}{2}) = \frac{1}{\Delta z}\delta_z v_2^{n+1}(i,j+\tfrac{1}{2},k+\tfrac{1}{2}) + \frac{1}{\Delta y}\delta_y v_3^{n+1}(i,j+\tfrac{1}{2},k+\tfrac{1}{2}), \tag{25c}$$

$$\sigma_x^{n+1}(i,j,k) = \lambda[\varepsilon_x^{n+1}(i,j,k)+\varepsilon_y^{n+1}(i,j,k)+\varepsilon_z^{n+1}(i,j,k)] + 2\mu\varepsilon_x^{n+1}(i,j,k) - (3\lambda+2\mu)\alpha_T[T_1^{n+1}(i,j,k)-T_0], \tag{26a}$$

$$\sigma_y^{n+1}(i,j,k) = \lambda[\varepsilon_x^{n+1}(i,j,k)+\varepsilon_y^{n+1}(i,j,k)+\varepsilon_z^{n+1}(i,j,k)] + 2\mu\varepsilon_y^{n+1}(i,j,k) - (3\lambda+2\mu)\alpha_T[T_1^{n+1}(i,j,k)-T_0], \tag{26b}$$

$$\sigma_z^{n+1}(i,j,k) = \lambda[\varepsilon_x^{n+1}(i,j,k)+\varepsilon_y^{n+1}(i,j,k)+\varepsilon_z^{n+1}(i,j,k)] + 2\mu\varepsilon_z^{n+1}(i,j,k) - (3\lambda+2\mu)\alpha_T[T_1^{n+1}(i,j,k)-T_0], \tag{26c}$$

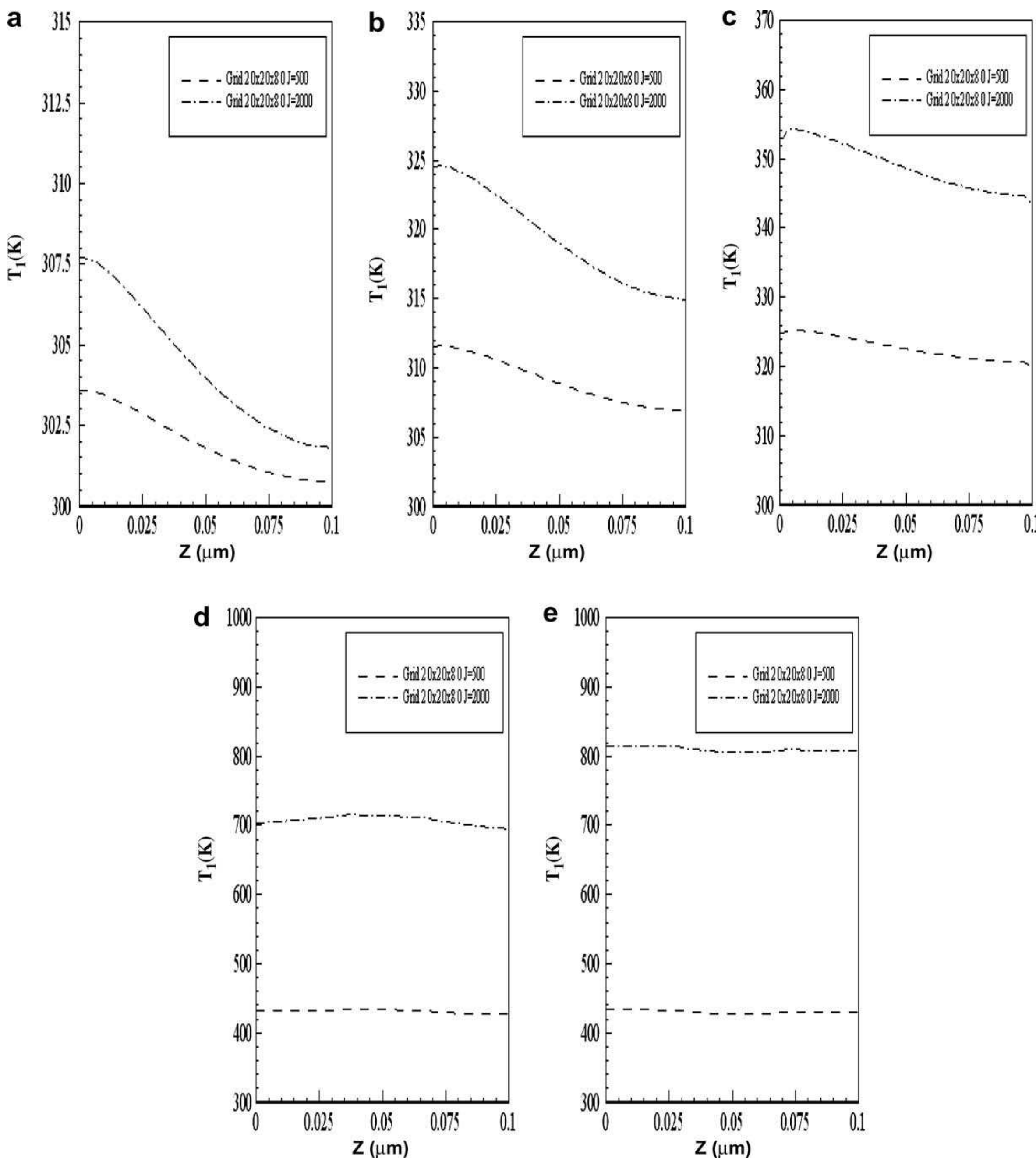

Fig. 5. Lattice temperature profiles along z at (x_{center}, y_{center}) at different times: (a) $t = 0.25$ ps, (b) $t = 0.5$ ps, (c) $t = 1$ ps, (d) $t = 10$ ps and (e) $t = 20$ ps with a mesh of $20 \times 20 \times 80$ and two different laser fluences J of 500 J/m^2 and J of 2000 J/m^2.

$$\sigma_{xy}^{n+1}(i+\tfrac{1}{2},j+\tfrac{1}{2},k)=\mu\gamma_{xy}^{n+1}(i+\tfrac{1}{2},j+\tfrac{1}{2},k), \tag{27a}$$

$$\sigma_{xz}^{n+1}(i+\tfrac{1}{2},j,k+\tfrac{1}{2})=\mu\gamma_{xz}^{n+1}(i+\tfrac{1}{2},j,k+\tfrac{1}{2}), \tag{27b}$$

$$\sigma_{yz}^{n+1}(i,j+\tfrac{1}{2},k+\tfrac{1}{2})=\mu\gamma_{yz}^{n+1}(i,j+\tfrac{1}{2},k+\tfrac{1}{2}), \tag{27c}$$

$$\begin{aligned}
C_{e0}\frac{T_e^{n+1}(i,j,k)+T_e^{n}(i,j,k)}{2T_0}\cdot\frac{1}{\Delta t}\Delta_{-t}T_e^{n+1}(i,j,k)
&=\frac{1}{2\Delta x^2}[k_e^{n+1}(i+\tfrac{1}{2},j,k)\delta_x T_e^{n+1}(i+\tfrac{1}{2},j,k)\\
&\quad-k_e^{n+1}(i-\tfrac{1}{2},j,k)\delta_x T_e^{n+1}(i-\tfrac{1}{2},j,k)]\\
&\quad+\frac{1}{2\Delta x^2}[k_e^{n}(i+\tfrac{1}{2},j,k)\delta_x T_e^{n}(i+\tfrac{1}{2},j,k)\\
&\quad-k_e^{n}(i-\tfrac{1}{2},j,k)\delta_x T_e^{n}(i-\tfrac{1}{2},j,k)]\\
&\quad+\frac{1}{2\Delta y^2}[k_e^{n+1}(i,j+\tfrac{1}{2},k)\delta_y T_e^{n+1}(i,j+\tfrac{1}{2},k)\\
&\quad-k_e^{n+1}(i,j-\tfrac{1}{2},k)\delta_y T_e^{n+1}(i,j-\tfrac{1}{2},k)]\\
&\quad+\frac{1}{2\Delta y^2}[k_e^{n}(i,j+\tfrac{1}{2},k)\delta_y T_e^{n}(i,j+\tfrac{1}{2},k)\\
&\quad-k_e^{n}(i,j-\tfrac{1}{2},k)\delta_y T_e^{n}(i,j-\tfrac{1}{2},k)]
\end{aligned}$$

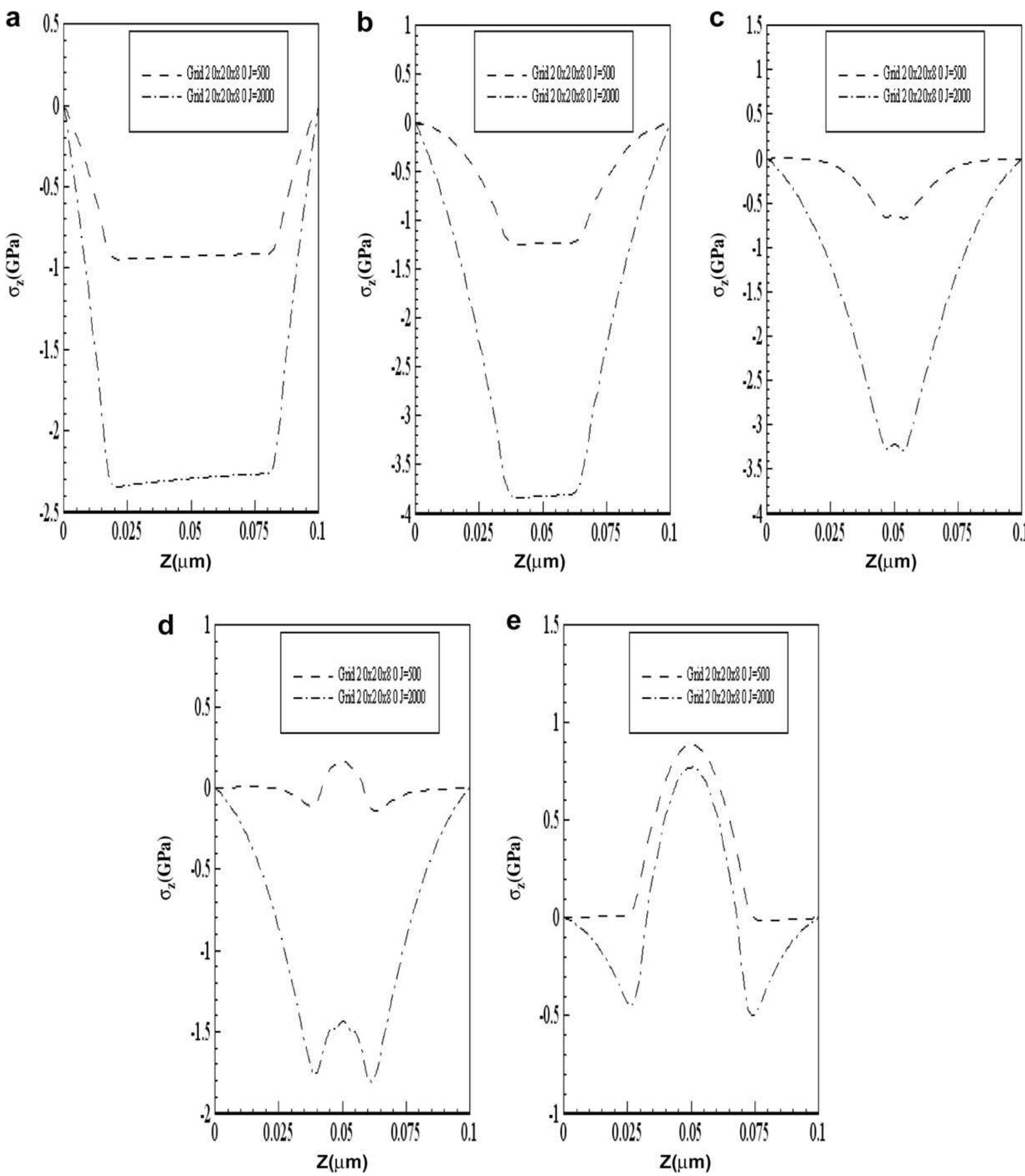

Fig. 6. Normal stress (σ_z) profiles along z at (x_{center}, y_{center}) at different times: (a) $t=5$ ps, (b) $t=10$ ps, (c) $t=15$ ps, (d) $t=17$ ps and (e) $t=20$ ps with a mesh of $20\times20\times80$ and two different laser fluences J of 500 J/m^2 and 2000 J/m^2.

$$
\begin{aligned}
&+\frac{1}{2\Delta z^2}[k_\mathrm{e}^{n+1}(i,j,k+\tfrac{1}{2})\delta_z T_\mathrm{e}^{n+1}(i,j,k+\tfrac{1}{2}) \\
&-k_\mathrm{e}^{n+1}(i,j,k-\tfrac{1}{2})\delta_z T_\mathrm{e}^{n+1}(i,j,k-\tfrac{1}{2})] \\
&+\frac{1}{2\Delta z^2}[k_\mathrm{e}^{n}(i,j,k+\tfrac{1}{2})\delta_z T_\mathrm{e}^{n}(i,j,k+\tfrac{1}{2}) \\
&-k_\mathrm{e}^{n}(i,j,k-\tfrac{1}{2})\delta_z T_\mathrm{e}^{n}(i,j,k-\tfrac{1}{2})] \\
&-G\left[\frac{T_\mathrm{e}^{n+1}(i,j,k)+T_\mathrm{e}^{n}(i,j,k)}{2}-\frac{T_\mathrm{l}^{n+1}(i,j,k)+T_\mathrm{l}^{n}(i,j,k)}{2}\right] \\
&+Q^{n+\frac{1}{2}}(i,j,k), \qquad (28)
\end{aligned}
$$

$$
\begin{aligned}
&C_\mathrm{l}\frac{1}{\Delta t}\Delta_{-t}T_\mathrm{l}^{n+1}(i,j,k) \\
&\quad=G\left[\frac{T_\mathrm{e}^{n+1}(i,j,k)+T_\mathrm{e}^{n}(i,j,k)}{2}-\frac{T_\mathrm{l}^{n+1}(i,j,k)+T_\mathrm{l}^{n}(i,j,k)}{2}\right] \\
&\quad-(3\lambda+2\mu)\alpha_\mathrm{T}T_0\frac{1}{\Delta t}[\Delta_{-t}\varepsilon_x^{n+1}(i,j,k)+\Delta_{-t}\varepsilon_y^{n+1}(i,j,k) \\
&\quad+\Delta_{-t}\varepsilon_z^{n+1}(i,j,k)], \qquad (29)
\end{aligned}
$$

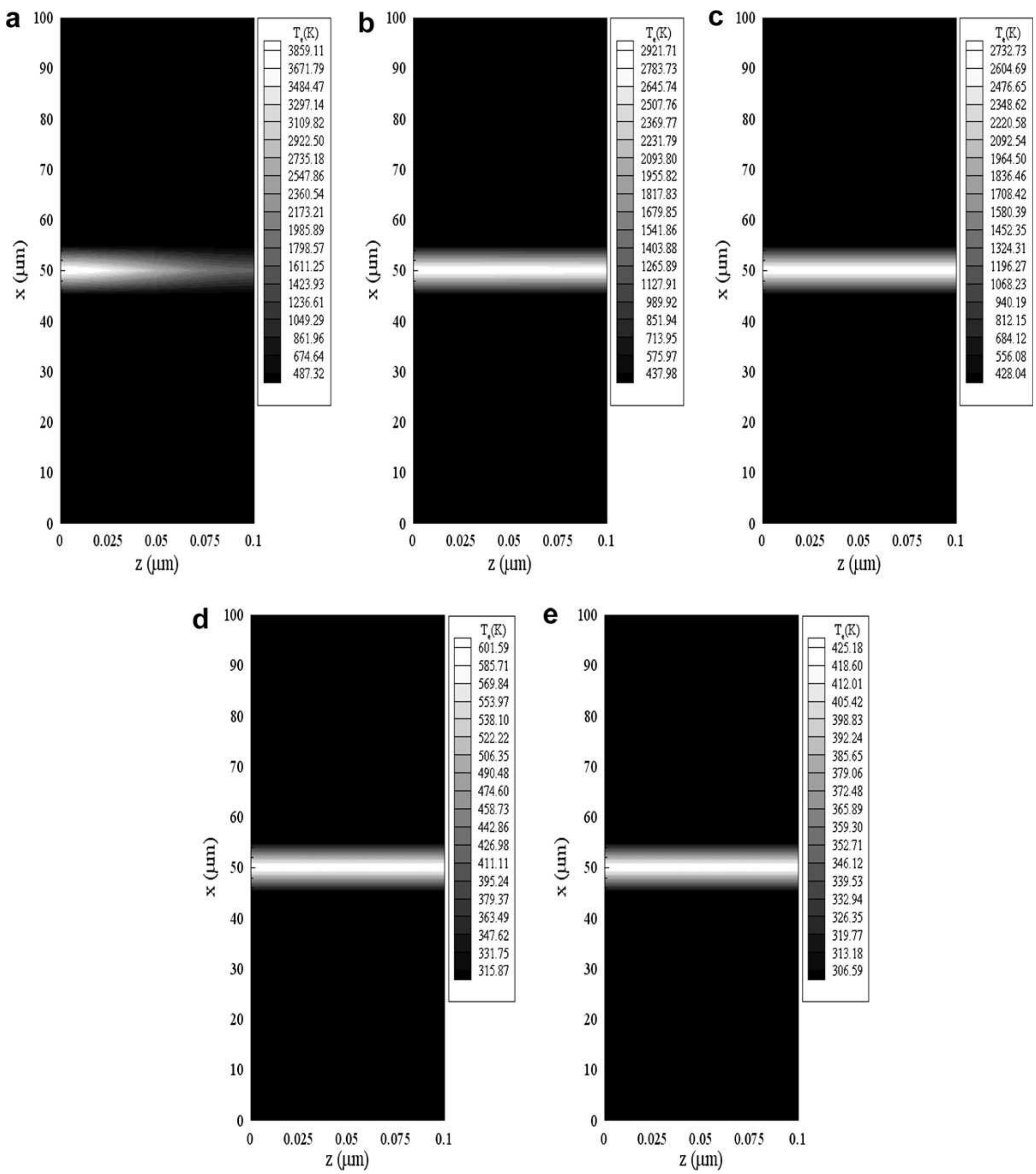

Fig. 7. Contours of electron temperature profiles in the cross-section of $y = 50$ μm at different times: (a) $t = 0.25$ ps, (b) $t = 0.5$ ps, (c) $t = 1$ ps, (d) $t = 10$ ps, and (e) $t = 20$ ps with a mesh of $20 \times 20 \times 80$ and laser fluence J of 500 $\mathrm{J/m^2}$.

$$\frac{1}{\Delta t}\Delta_{-t}u^{n+1}(i+\tfrac{1}{2},j,k) = v_1^{n+1}(i+\tfrac{1}{2},j,k), \tag{30a}$$

$$\frac{1}{\Delta t}\Delta_{-t}v^{n+1}(i,j+\tfrac{1}{2},k) = v_2^{n+1}(i,j+\tfrac{1}{2},k), \tag{30b}$$

$$\frac{1}{\Delta t}\Delta_{-t}w^{n+1}(i,j,k+\tfrac{1}{2}) = v_3^{n+1}(i,j,k+\tfrac{1}{2}). \tag{30c}$$

To complete the formulation of our numerical method, we now turn our attention to the approximation of boundary and initial conditions:

$$\sigma_x^n(1,j,k) = \sigma_x^n(N_x+1,j,k) = 0,\quad 1 \leqslant j \leqslant N_y+1, 1 \leqslant k \leqslant N_z+1; \tag{31a}$$

$$\sigma_{xy}^n(1+\tfrac{1}{2},j+\tfrac{1}{2},k) = \sigma_{xy}^n(N_x+\tfrac{1}{2},j+\tfrac{1}{2},k) = 0,\quad 1 \leqslant j \leqslant N_y,\ 1 \leqslant k \leqslant N_z; \tag{31b}$$

$$\sigma_{xz}^n(1+\tfrac{1}{2},j,k+\tfrac{1}{2}) = \sigma_{xz}^n(N_x+\tfrac{1}{2},j,k+\tfrac{1}{2}) = 0,\quad 1 \leqslant j \leqslant N_y,\ 1 \leqslant k \leqslant N_z; \tag{31c}$$

$$\sigma_{yz}^n(1,j+\tfrac{1}{2},k+\tfrac{1}{2}) = \sigma_{yz}^n(N_x,j+\tfrac{1}{2},k+\tfrac{1}{2}) = 0,\quad 1 \leqslant j \leqslant N_y,\ 1 \leqslant k \leqslant N_z; \tag{31d}$$

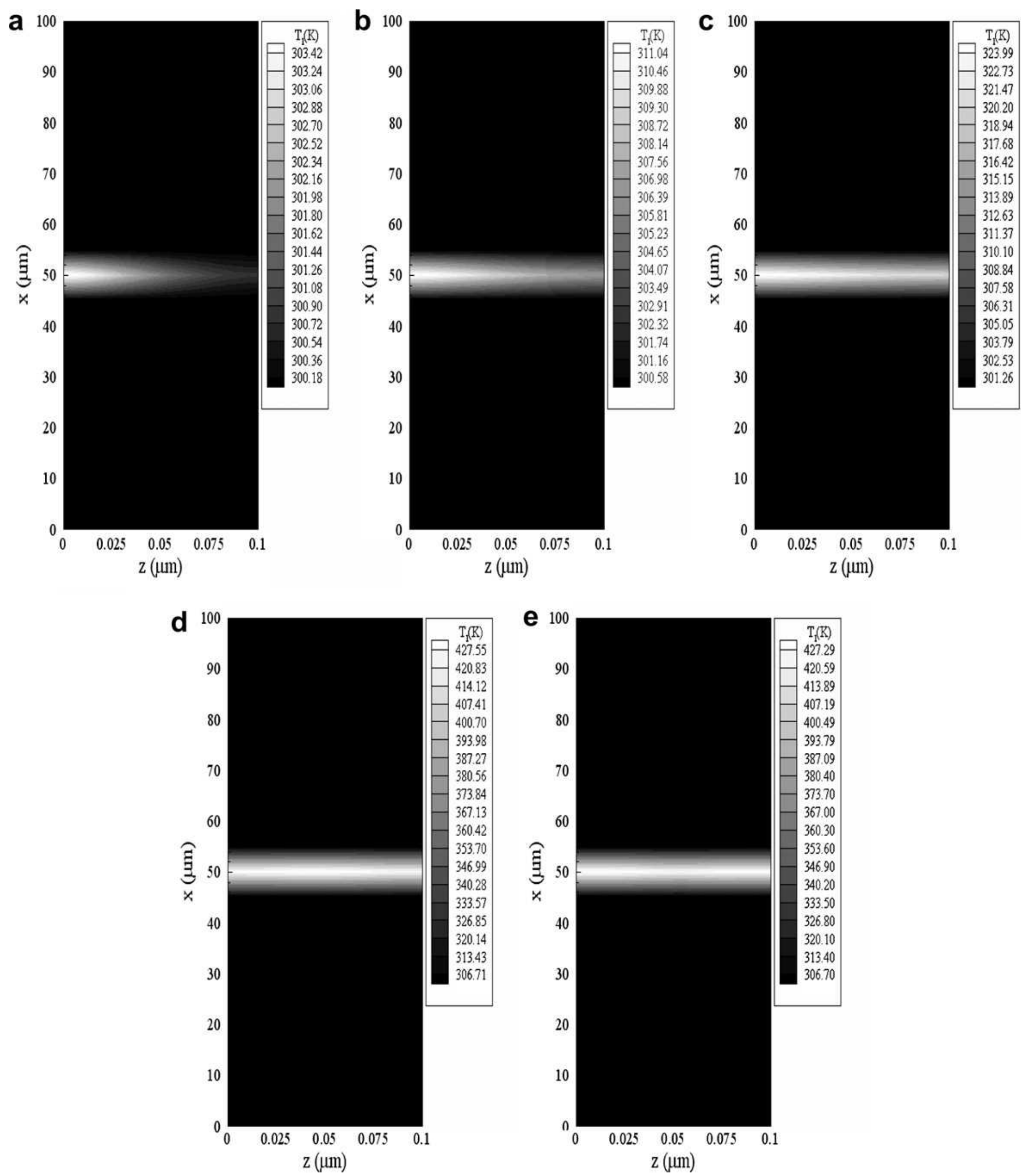

Fig. 8. Contours of lattice temperature profiles in the cross-section of $y = 50$ μm at different times: (a) $t = 0.25$ ps, (b) $t = 0.5$ ps, (c) $t = 1$ ps, (d) $t = 10$ ps, and (e) $t = 20$ ps with a mesh of $20 \times 20 \times 80$ and laser fluence J of 500 J/m^2.

$$\sigma_y^n(i,1,k) = \sigma_y^n(i,N_y+1,k) = 0,$$
$$1 \leqslant i \leqslant N_x+1,\ 1 \leqslant k \leqslant N_z+1; \tag{32a}$$
$$\sigma_{xy}^n(i+\tfrac{1}{2},1+\tfrac{1}{2},k) = \sigma_{xy}^n(i+\tfrac{1}{2},N_y+\tfrac{1}{2},k) = 0,$$
$$1 \leqslant i \leqslant N_x,\ 1 \leqslant k \leqslant N_z; \tag{32b}$$
$$\sigma_{xz}^n(i+\tfrac{1}{2},1,k+\tfrac{1}{2}) = \sigma_{xz}^n(i+\tfrac{1}{2},N_y,k+\tfrac{1}{2}) = 0,$$
$$1 \leqslant i \leqslant N_x,\ 1 \leqslant k \leqslant N_z; \tag{32c}$$
$$\sigma_{yz}^n(i,1+\tfrac{1}{2},k+\tfrac{1}{2}) = \sigma_{yz}^n(i,N_y+\tfrac{1}{2},k+\tfrac{1}{2}) = 0,$$
$$1 \leqslant i \leqslant N_x,\ 1 \leqslant k \leqslant N_z; \tag{32d}$$

$$\sigma_z^n(i,j,1) = \sigma_z^n(i,j,N_z+1) = 0,$$
$$1 \leqslant i \leqslant N_x+1,\ 1 \leqslant j \leqslant N_y+1; \tag{33a}$$
$$\sigma_{xy}^n(i+\tfrac{1}{2},j+\tfrac{1}{2},1) = \sigma_{xy}^n(i+\tfrac{1}{2},j+\tfrac{1}{2},N_z) = 0,$$
$$1 \leqslant i \leqslant N_x,\ 1 \leqslant j \leqslant N_y; \tag{33b}$$
$$\sigma_{xz}^n(i+\tfrac{1}{2},j,1+\tfrac{1}{2}) = \sigma_{xz}^n(i+\tfrac{1}{2},j,N_z+\tfrac{1}{2}) = 0,$$
$$1 \leqslant i \leqslant N_x,\ 1 \leqslant j \leqslant N_y; \tag{33c}$$
$$\sigma_{yz}^n(i,j+\tfrac{1}{2},1+\tfrac{1}{2}) = \sigma_{yz}^n(i,j+\tfrac{1}{2},N_z+\tfrac{1}{2}) = 0,$$
$$1 \leqslant i \leqslant N_x,\ 1 \leqslant j \leqslant N_y; \tag{33d}$$

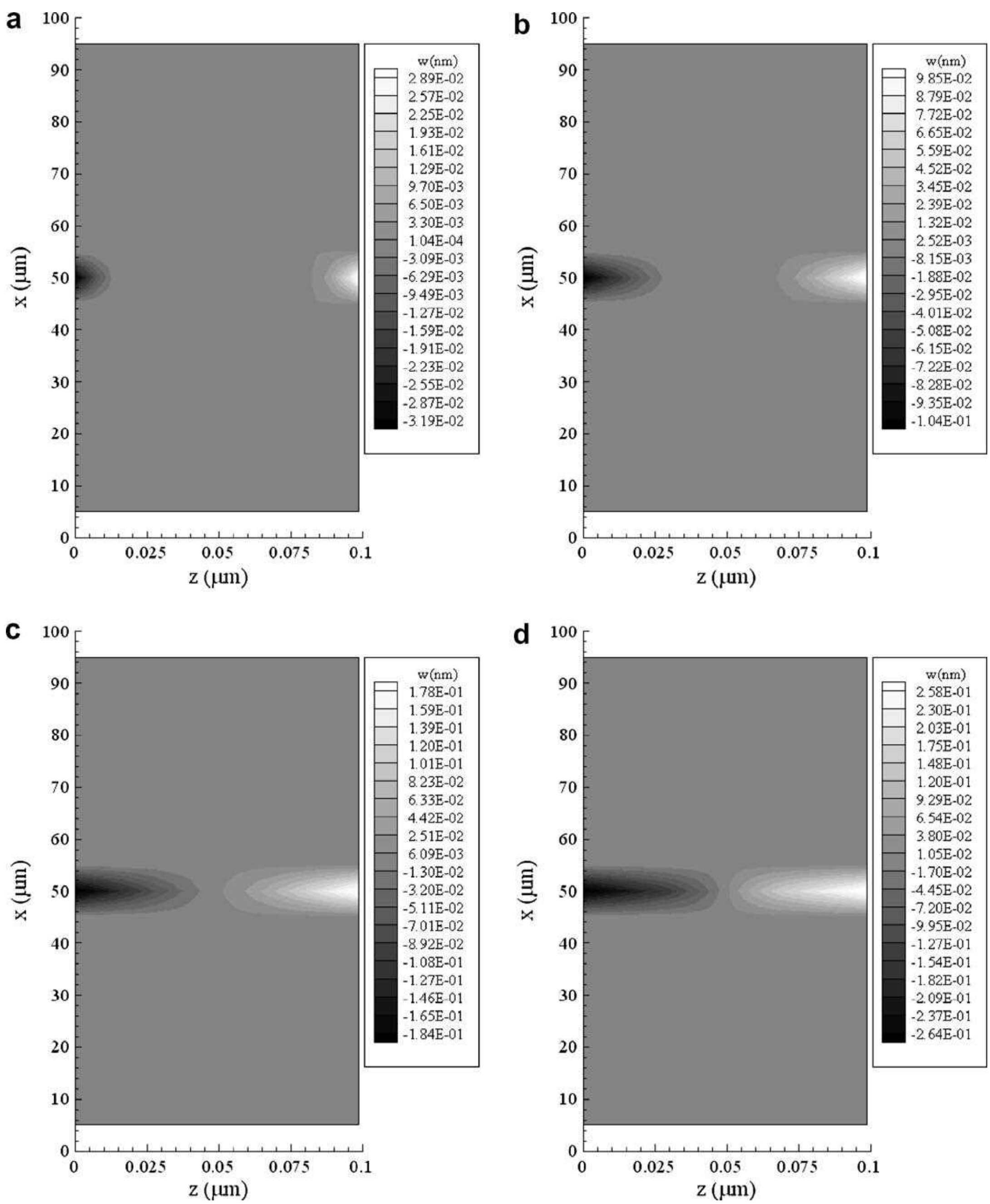

Fig. 9. Contours of displacement (w) profiles in the cross-section of $y = 50$ μm at different times: (a) $t = 5$ ps, (b) $t = 10$ ps, (c) $t = 15$ ps, and (d) $t = 20$ ps with a mesh of $20 \times 20 \times 80$ and laser fluence J of 500 J/m^2.

$$T_e^n(1,j,k) = T_e^n(2,j,k), \quad T_e^n(N_x+1,j,k) = T_e^n(N_x,j,k); \tag{34a}$$

$$T_e^n(i,1,k) = T_e^n(i,2,k), \quad T_e^n(i,N_y+1,k) = T_e^n(i,N_y,k); \tag{34b}$$

$$T_e^n(i,j,1) = T_e^n(i,j,2), \quad T_e^n(i,j,N_z+1) = T_e^n(i,j,N_z); \tag{34c}$$

$$T_l^n(1,j,k) = T_l^n(2,j,k), \quad T_l^n(N_x+1,j,k) = T_l^n(N_x,j,k); \tag{35a}$$

$$T_l^n(i,1,k) = T_l^n(i,2,k), \quad T_l^n(i,N_y+1,k) = T_l^n(i,N_y,k); \tag{35b}$$

$$T_l^n(i,j,1) = T_l^n(i,j,2), \quad T_l^n(i,j,N_z+1) = T_l^n(i,j,N_z), \tag{35c}$$

where $1 \leqslant i \leqslant N_x+1$, $1 \leqslant j \leqslant N_y+1$, $1 \leqslant k \leqslant N_z+1$, for any time level n. The initial conditions are approximated as

$$u^0(i+\tfrac{1}{2},j,k) = v^0(i,j+\tfrac{1}{2},k) = w^0(i,j,k+\tfrac{1}{2}) = 0, \tag{36a}$$

$$v_1^0(i+\tfrac{1}{2},j,k) = v_2^0(i,j+\tfrac{1}{2},k) = v_3^0(i,j,k+\tfrac{1}{2}) = 0, \tag{36b}$$

$$T_e^0(i,j,k) = T_l^0(i,j,k) = T_0, \tag{36c}$$

$$\varepsilon_x^0(i+\tfrac{1}{2},j,k) = \varepsilon_y^0(i,j+\tfrac{1}{2},k) = \varepsilon_z^0(i,j,k+\tfrac{1}{2}) = 0, \tag{36d}$$

$$\sigma_x^0(i+\tfrac{1}{2},j,k) = \sigma_y^0(i,j+\tfrac{1}{2},k) = \sigma_z^0(i,j,k+\tfrac{1}{2}) = 0, \tag{36e}$$

$$\sigma_{xy}^0(i+\tfrac{1}{2},j+\tfrac{1}{2},k) = \gamma_{xy}^0(i+\tfrac{1}{2},j+\tfrac{1}{2},k) = 0, \tag{36f}$$

$$\sigma_{xz}^0(i+\tfrac{1}{2},j,k+\tfrac{1}{2}) = \gamma_{xz}^0(i+\tfrac{1}{2},j,k+\tfrac{1}{2}) = 0, \tag{36g}$$

$$\sigma_{yz}^0(i,j+\tfrac{1}{2},k+\tfrac{1}{2}) = \gamma_{yz}^0(i,j+\tfrac{1}{2},k+\tfrac{1}{2}) = 0. \tag{36h}$$

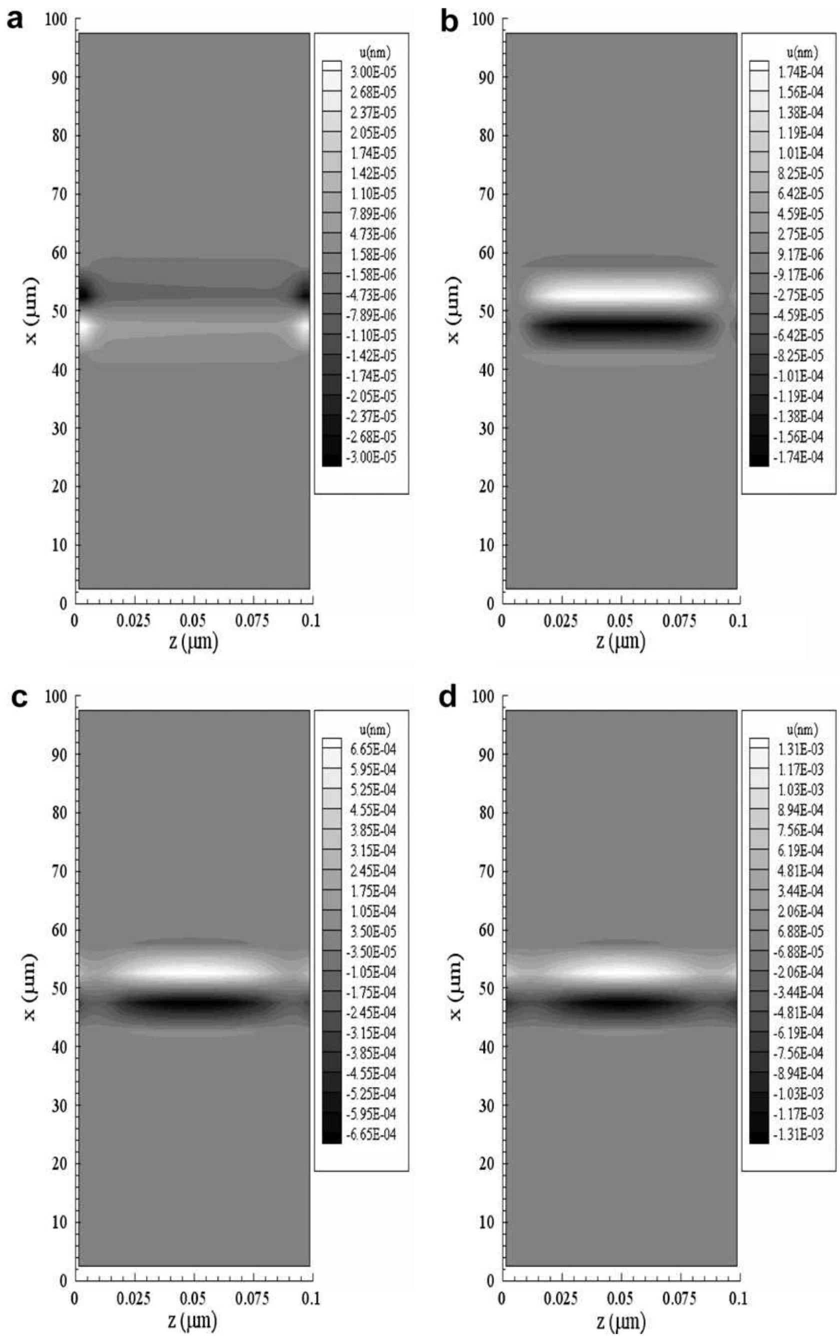

Fig. 10. Contours of displacement (u) profiles in the cross-section of $y = 50$ μm at different times: (a) $t = 5$ ps, (b) $t = 10$ ps, (c) $t = 15$ ps, and (d) $t = 20$ ps with a mesh of $20 \times 20 \times 80$ and laser fluence J of 500 J/m^2.

where $1 \leqslant i \leqslant N_x+1,\ 1 \leqslant j \leqslant N_y+1,\ 1 \leqslant k \leqslant N_z+1$, for any time level n.

It should be pointed out that Eqs. (21)–(23) are nonlinear since the terms $\delta_x(T_e^2)^{n+1}(i+\frac{1}{2},j,k)$, $\delta_y(T_e^2)^{n+1}(i,j+\frac{1}{2},k)$ and $\delta_z(T_e^2)^{n+1}(i,j,k+\frac{1}{2})$ are nonlinear. Also, it can be seen that Eq. (28) is nonlinear. Therefore, the above scheme must be solved iteratively. An iterative method for solving the above scheme at time level $n+1$ is developed as follows:

Step 1. Set the values ε_x^{n+1}, ε_y^{n+1}, ε_z^{n+1}, γ_{xy}^{n+1}, γ_{xz}^{n+1} and γ_{yz}^{n+1}, solve Eqs. (28) and (29) iteratively for T_e^{n+1} and T_l^{n+1}.

Step 2. Solve for σ_x^{n+1}, σ_y^{n+1}, σ_z^{n+1}, σ_{xy}^{n+1}, σ_{xz}^{n+1} and σ_{yz}^{n+1} using Eqs. (26) and (27).

Step 3. Solve for derivatives of σ_x^{n+1}, σ_y^{n+1}, σ_z^{n+1}, σ_{xy}^{n+1}, σ_{xz}^{n+1} and σ_{yz}^{n+1} using Eqs. (19), (20) or similar equations.

Step 4. Solve for v_1^{n+1}, v_2^{n+1} and v_3^{n+1} using Eqs. (21)–(23).

Step 5. Update ε_x^{n+1}, ε_y^{n+1}, ε_z^{n+1}, γ_{xy}^{n+1}, γ_{xz}^{n+1} and γ_{yz}^{n+1} using Eqs. (24) and (25).

Given the required accuracy ϵ_1 (for temperature) and ϵ_2 (for strain), repeat the above steps until a convergent solution is obtained based on the following criteria

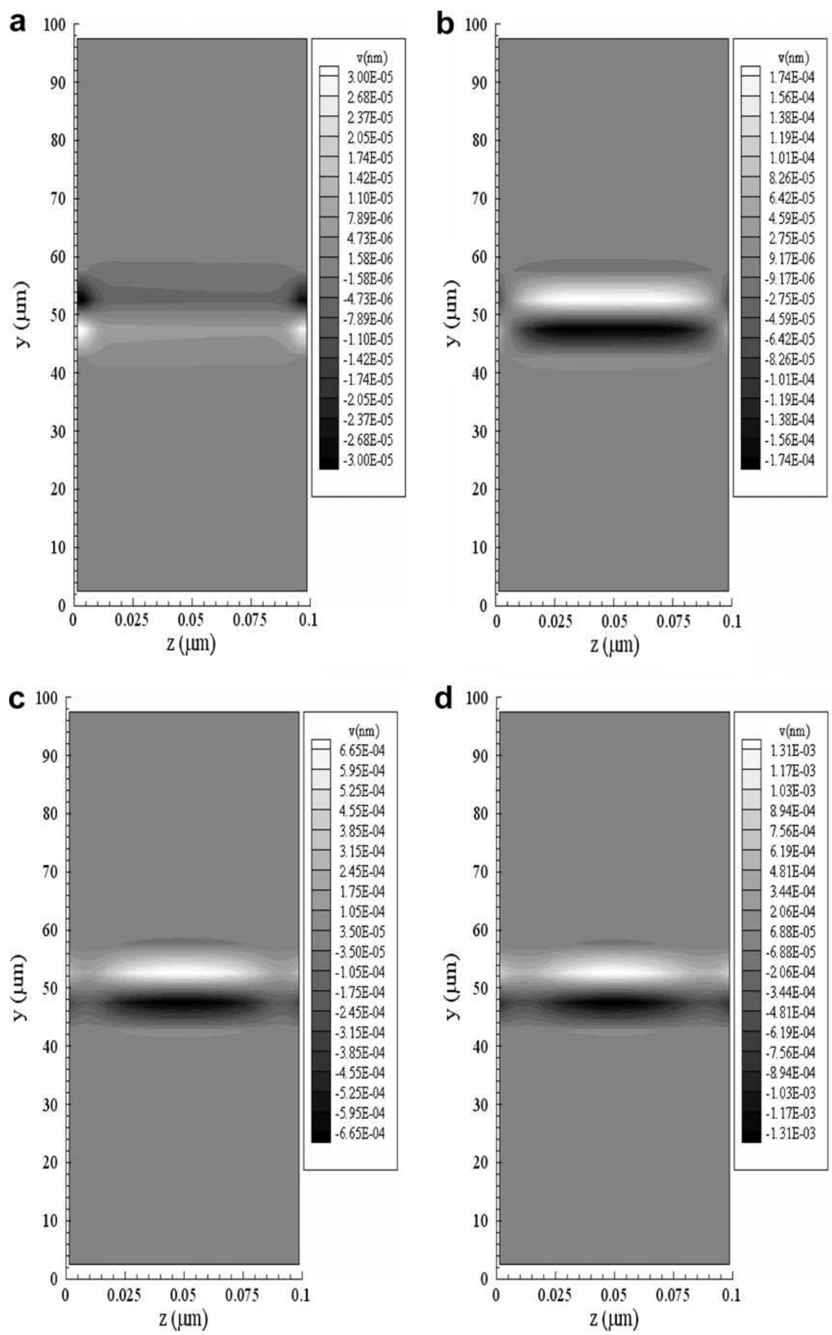

Fig. 11. Contours of displacement (v) profiles in the cross-section of $x = 50$ μm at different times: (a) $t = 5$ ps, (b) $t = 10$ ps, (c) $t = 15$ ps, and (d) $t = 20$ ps with a mesh of $20 \times 20 \times 80$ and laser fluence J of 500 J/m^2.

$$|T_e^{n+1}(i,j,k) - T_e^n(i,j,k)| \leqslant \epsilon_1, \tag{37a}$$

$$|\varepsilon_x^{n+1}(i,j,k) - \varepsilon_x^n(i,j,k)| \leqslant \epsilon_2, \quad |\varepsilon_y^{n+1}(i,j,k) - \varepsilon_y^n(i,j,k)| \leqslant \epsilon_2, \tag{37b}$$

$$|\varepsilon_z^{n+1}(i,j,k) - \varepsilon_z^n(i,j,k)| \leqslant \epsilon_2, \quad |\gamma_{xy}^{n+1}(i,j,k) - \gamma_{xy}^n(i,j,k)| \leqslant \epsilon_2, \tag{37c}$$

$$|\gamma_{xz}^{n+1}(i,j,k) - \gamma_{xz}^n(i,j,k)| \leqslant \epsilon_2, \quad |\gamma_{yz}^{n+1}(i,j,k) - \gamma_{yz}^n(i,j,k)| \leqslant \epsilon_2. \tag{37d}$$

4. Numerical examples

To test the applicability of the developed numerical scheme, we investigated the temperature rise and thermal deformation in a thin film with the dimensions 100 μm × 100 μm × 0.1 μm, as shown in Fig. 1. The thermophysical properties for gold are listed in Table 1 [1,24,35]. Three meshes of 20 × 20 × 40, 20 × 20 × 80, 20 × 20 × 100 were chosen in order to test the convergence of the scheme. The time increment was chosen to be 0.005 ps and T_0 was set to

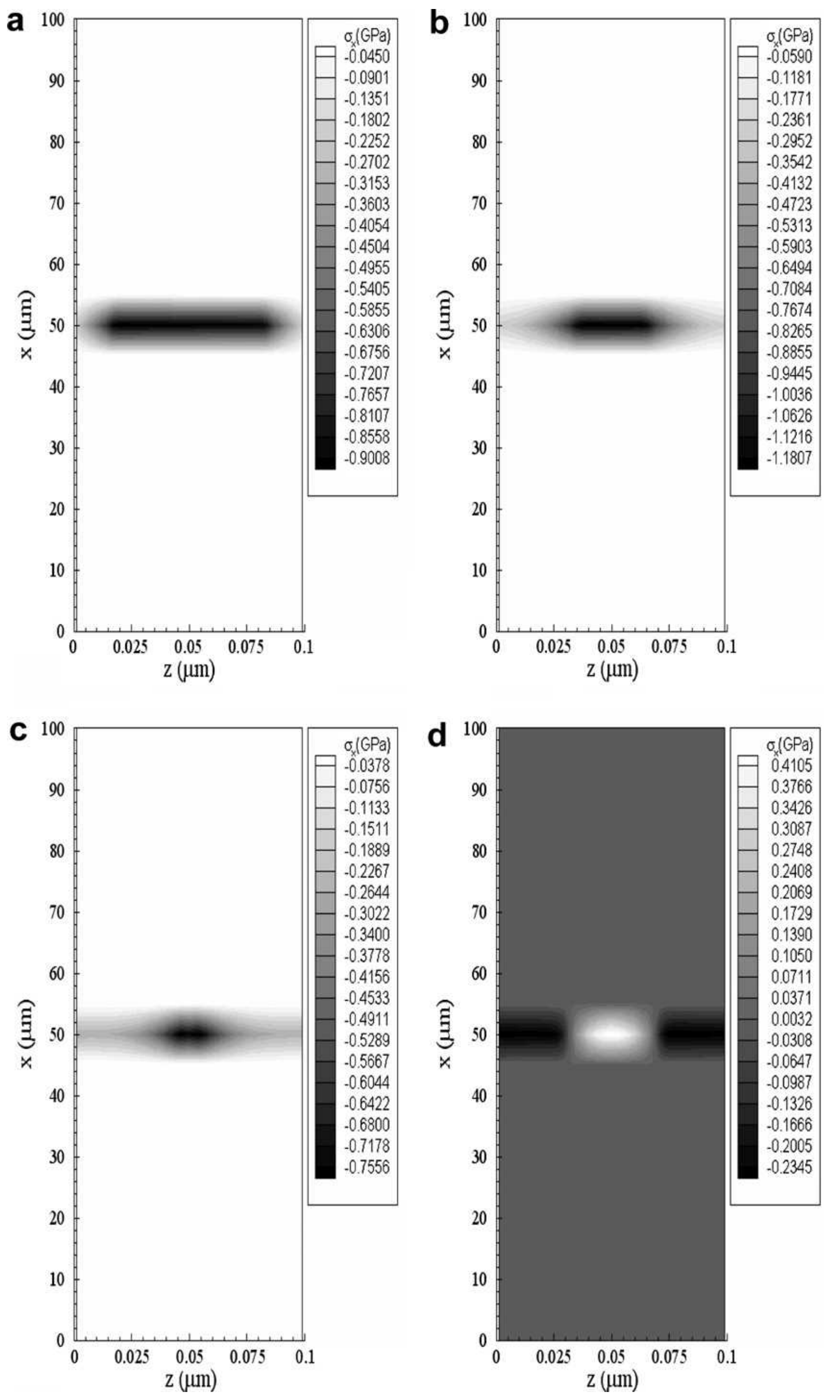

Fig. 12. Contours of normal stress (σ_x) profiles in the cross-section of $y = 50$ μm at different times: (a) $t = 5$ ps, (b) $t = 10$ ps, (c) $t = 15$ ps, and (d) $t = 20$ ps with a mesh of 20 × 20 × 80 and laser fluence J of 500 J/m^2.

be 300 K. Two different values of laser fluences ($J = 500$ J/m^2, 2000 J/m^2) were chosen to study the hot electron-blast force. The convergence criteria were chosen to be $\epsilon_1 = 10^{-8}$ for temperature and $\epsilon_2 = 10^{-16}$ for deformation.

We assumed that the laser was focused on the center of the film surface. Fig. 3a shows the change in electron temperature $(\Delta T_e/(\Delta T_e)_{max})$ at the center ($x_{center} = 50$ μm, $y_{center} = 50$ μm and $z = 0$ μm) with laser fluences $J = 500$ J/m^2. The maximum temperature rise of T_e (i.e., $(\Delta T_e)_{max}$) is about 3763 K, which is close to that obtained in [34]. Fig. 3b shows the displacement (w) at the center (x_{center}, y_{center}, z) versus time. It can be seen from both figures that mesh size had no significant effect on the solution and hence the solution is convergent.

Figs. 4 and 5 show electron temperature and lattice temperature along z at (x_{center}, y_{center}) with two different laser fluences ($J = 500$ J/m^2 and 2000 J/m^2) at different times (a) $t = 0.25$ ps, (b) $t = 0.5$ ps, (c) $t = 1$ ps, (d) $t = 10$ ps,

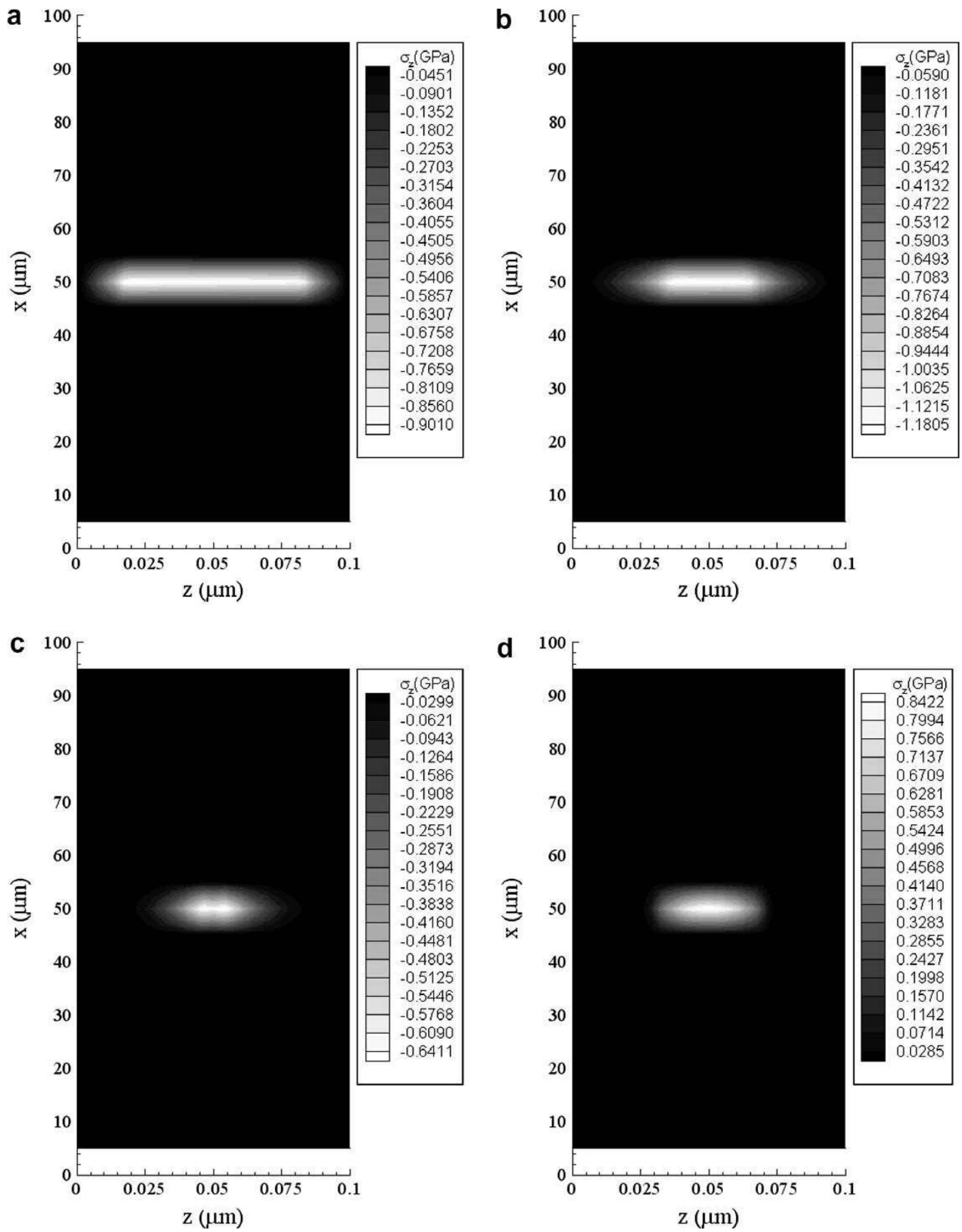

Fig. 13. Contours of normal stress (σ_z) profiles in the cross-section of $y = 50$ μm at different times: (a) $t = 5$ ps, (b) $t = 10$ ps, (c) $t = 15$ ps, and (d) $t = 20$ ps with a mesh of $20 \times 20 \times 80$ and laser fluence J of 500 J/m^2.

and (e) $t = 20$ ps, respectively. It can be seen that the electron temperature rises to its maximum at the beginning and then decreases while the lattice temperature rises gradually with time.

Fig. 6 shows normal stress σ_z along z at (x_{center}, y_{center}) at different times (a) $t = 5$ ps, (b) $t = 10$ ps, (c) $t = 15$ ps, (d) $t = 17$ ps and (e) $t = 20$ ps with a mesh of $20 \times 20 \times 80$ and two different laser fluences ($J = 500\ \text{J/m}^2$ and $2000\ \text{J/m}^2$). Usually, numerical oscillations appear near the peak of the curve, as shown in Fig. 5 [27]. It can be seen from Fig. 6 (particularly, Fig. 6d–e) that the normal stress σ_z does not show non-physical oscillations near the peak of the curve.

Figs. 7–14 were plotted based on the results obtained in a mesh of $20 \times 20 \times 80$ with a laser fluence of $J = 500\ \text{J/m}^2$. Figs. 7 and 8 show contours of electron temperature profile and lattice temperature profile in the cross-section of $y = y_{\text{center}}$ at different times (a) $t = 0.25$ ps,

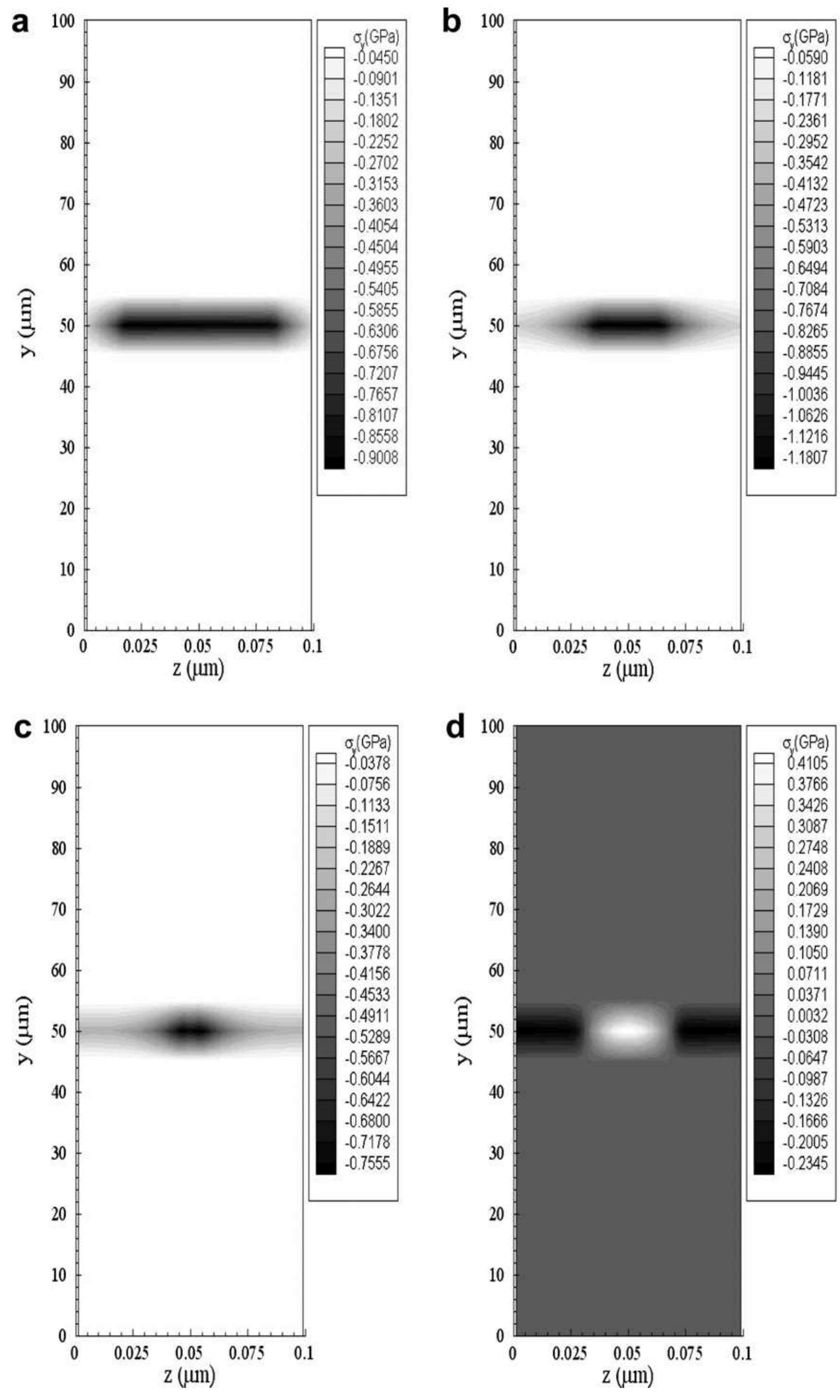

Fig. 14. Contours of normal stress (σ_y) profiles in the cross-section of $x = 50$ μm at different times: (a) $t = 5$ ps, (b) $t = 10$ ps, (c) $t = 15$ ps, and (d) $t = 20$ ps with a mesh of $20 \times 20 \times 80$ and laser fluence J of $500\ \text{J/m}^2$.

(b) $t = 0.5$ ps, (c) $t = 1$ ps, (d) $t = 10$ ps, and (e) $t = 20$ ps, respectively. It can be seen from both figures that the heat is mainly transferred along the z direction. This result illustrates the fact that the femtosecond lasers are an ideal candidate for precise thermal processing of functional nanophase materials. Figs. 9–14 show contours of displacements (u, v, w) and normal stresses $(\sigma_x, \sigma_y, \sigma_z)$ in the cross-section of $y = y_{\text{center}}$ at different times (a) $t = 5$ ps, (b) $t = 10$ ps, (c) $t = 15$ ps, and (d) $t = 20$ ps, respectively. It can be seen from Figs. 9–11 that the central part of the film is expanding because displacement changes from negative to positive along the center line in the z direction, and along x and y directions, respectively. Similar stress alterations are observed from Figs. 12–14.

5. Conclusion

We have developed a finite difference method for studying thermal deformation in a 3D thin film exposed to ultrashort pulsed lasers. The method, based on the parabolic two-step heat transport equations, accounts for the coupling effect between lattice temperature and strain rate, as well as for the hot electron-blast effect in momentum transfer. By replacing the displacement components in the dynamic equations of motion using the velocity components, developing a fourth-order compact method for evaluating stress derivatives in the dynamic equations of motion, and employing a staggered grid, we have developed a numerical method that allows us to avoid non-physical oscillations in the solution. Numerical results show the displacement and stress alterations at the center along the z direction, and along x and y directions, which reveal that the central part of thin film expands. Further research will focus on 3D double-layered cases where the interface could be either perfect thermal contact or imperfect thermal contact.

References

[1] D.Y. Tzou, J.K. Chen, J.E. Beraun, Hot-electron blast induced by ultrashort-pulsed lasers in layered media, Int. J. Heat Mass Transfer 45 (2002) 3369–3382.

[2] A. Mandelis, S.B. Peralta, Thermal wave based materials characterization and nondestructive evaluation of high-temperature superconductors: a critical review, in: R. Kossowsky (Ed.), Physics and Materials Science of High Temperature Superconductors, vol. II, Kluwer Academic publishers, Boston, MA, 1992, pp. 413–440.

[3] J. Opsal, The application of thermal wave technology to thickness and grain size of aluminum films, in: Metallization: Performance and Reliability Issues for VLSI and ULSI, SPIE 1596 (1991) 120–131.

[4] D.J. Elliot, B.P. Piwczyk, Single and multiple pulse ablation of polymeric and high density materials with excimer laser radiation at 193 nm and 248 nm, Mater. Res. Soc. Symp. Proc. 129 (1989) 627–636.

[5] C.P. Grigoropoulos, Heat transfer in laser processing of thin films, in: C.L. Tien (Ed.), Annual Review of Heat Transfer, vol. V, Hemisphere, New York, 1994, pp. 77–130.

[6] J. Narayan, V.P. Gosbole, G.W. White, Laser method for synthesis and processing of continuous diamond films on nondiamond substrates, Science 252 (1991) 416–418.

[7] J.M. Hopkins, J. Sibbett, Ultrashort-pulse lasers: big payoffs in a flash, Sci. AM. 283 (2000) 72–79.

[8] J. Liu, Preliminary survey on the mechanisms of the wave-like behaviors of heat transfer in living tissues, Forsch. Ingenieurwes. 66 (2000) 1–10.

[9] C. Momma, S. Nolte, B.N. Chichkov, F.V. Alvensleben, A. Tunnermann, Precise laser ablation with ultrashort pulses, Appl. Surf. Sci. 109 (1997) 15–19.

[10] M.D. Shirk, P.A. Molian, A review of ultrashort pulsed laser ablation of materials, J. Laser Appl. 10 (1998) 18–28.

[11] A.N. Smith, J.L. Hostetler, P.M. Norris, Nonequilibrium heating in metal films: an analytical and numerical analysis, Numer. Heat Transfer Part A 35 (1999) 859–873.

[12] K. Fushinobu, L.M. Phinney, Y. Kurosaki, C.L. Tien, Optimization of laser parameters for ultrashort-pulse laser recovery of stiction-failed microstructures, Numer. Heat Transfer Part A 36 (1999) 345–357.

[13] J.K. Chen, J.E. Beraun, Numerical study of ultrashort laser pulse interactions with metal films, Numer. Heat Transfer Part A 40 (2001) 1–20.

[14] E. Hoashi, T. Yokomine, A. Shimizu, Numerical analysis of ultrafast heat with phase change in a material irradiated by an ultrashort pulsed laser, Numer. Heat Transfer Part A 41 (2002) 783–801.

[15] S.H. Lee, J.S. Lee, S. Park, Y.K. Choi, Numerical analysis on heat transfer characteristics of a silicon film irradiated by pico-to femtosecond pulse lasers, Numer. Heat Transfer Part A 44 (2003) 833–850.

[16] S.H. Lee, K.G. Kang, Numerical analysis of electronic transport characteristics in dielectrics irradiated by ultrashort pulsed laser using the nonlocal Fokker–Planck equation, Numer. Heat Transfer Part A 48 (2005) 59–76.

[17] J.K. Chen, W.P. Latham, J.E. Beraun, Axisymmetric modeling of femtosecond-pulse laser heating on metal films, Numer. Heat Transfer Part B 42 (2002) 1–17.

[18] B. Xu, B.Q. Li, Finite element solution of non-Fourier thermal wave problems, Numer. Heat Transfer Part B 44 (2003) 45–60.

[19] W. Dai, H. Song, S. Su, R. Nassar, A stable finite difference scheme for solving a hyperbolic two-step model in a 3D micro-sphere heated by ultrashort-pulsed lasers, Int. J. Numer. Meth. Heat Fluid Flow 16 (2006) 693–717.

[20] B.R. Barron, W. Dai, A hybrid FE-FD scheme for solving parabolic two-step micro heat transport equations in an irregularly shaped three dimensional double-layered thin film, Numer. Heat Transfer Part B 49 (2006) 765–784.

[21] I. Kaba, W. Dai, A stable three-level finite difference scheme for solving the parabolic two-step model in a 3D micro-sphere heated by ultrashort-pulsed lasers, J. Comput. Appl. Math. 181 (2005) 125–147.

[22] W. Dai, G. Li, R. Nassar, L. Shen, An unconditionally stable three level finite difference scheme for solving parabolic two-step micro heat transport equations in a three-dimensional double-layered thin film, Int. J. Numer. Meth. Eng. 59 (2004) 493–509.

[23] J.K. Chen, D.Y. Tzou, J.E. Beraun, Numerical investigation of ultrashort laser damage in semiconductors, Int. J. Heat Mass Transfer 48 (2005) 501–509.

[24] J.K. Chen, J.E. Beraun, C.L. Tham, Comparison of one-dimensional and two-dimensional axisymmetric approaches to the thermomechanical response caused by ultrashort laser heating, J. Opt. A: Pure Appl. Opt. 4 (2002) 650–661.

[25] J.K. Chen, J.E. Beraun, C.L. Tham, Investigation of thermal response caused by pulse laser heating, Numer. Heat Transfer Part A 44 (2003) 705–722.

[26] J.K. Chen, J.E. Beraun, D.Y. Tzou, Thermomechanical response of metal films heated by ultrashort-pulsed lasers, J. Therm. Stresses 25 (2002) 539–558.

[27] H. Wang, W. Dai, R. Nassar, R.V.N. Melnik, A finite difference method for studying thermal deformation in a thin film exposed to ultrashort-pulsed lasers, Int. J. Heat Mass Transfer 49 (2006) 2712–2723.

[28] H. Wang, W. Dai, R.V.N. Melnik, A finite difference method for studying thermal deformation in a double-layered thin film exposed to ultrashort-pulsed lasers, Int. J. Therm. Sci. 46 (2006) 1179–1196.
[29] H. Wang, W. Dai, L.G. Hewavitharana, A finite difference method for studying thermal deformation in a double-layered thin film with imperfect interfacial contact exposed to ultrashort-pulsed lasers, Int. J. Therm. Sci. 47 (2008) 7–24.
[30] S.D. Brorson, J.G. Fujimoto, E.P. Ippen, Femtosecond electron heat transfer dynamics in thin gold film, Phys. Rev. Lett. 59 (1987) 1962–1965.
[31] H. Reismann, P.S. Pawlik, Elasticity, Theory and Applications, Wiley, New York, 1980, p. 135.
[32] T.Q. Qiu, C.L. Tien, Short-pulse laser heating on metals, Int. J. Heat Mass Transfer 35 (1992) 719–726.
[33] S.V. Patankar, Numerical Heat Transfer and Fluid Flow, McGraw-Hill, New York, 1980 (Chapter 5).
[34] T.Q. Qiu, C.L. Tien, Short-femtosecond laser heating of multi-layer metals I. Analysis, Int. J. Heat Mass Transfer 37 (1994) 2789–2797.
[35] G.W.C. Kaye, Tables of Physical and Chemical Constants and Some Mathematical Functions, 14th ed., Longman, London, UK, 1973, p. 31.